

We are IntechOpen, the world's leading publisher of Open Access books Built by scientists, for scientists

6,900

Open access books available

186,000

International authors and editors

200M

Downloads

Our authors are among the

154

Countries delivered to

TOP 1%

most cited scientists

12.2%

Contributors from top 500 universities



WEB OF SCIENCE™

Selection of our books indexed in the Book Citation Index
in Web of Science™ Core Collection (BKCI)

Interested in publishing with us?
Contact book.department@intechopen.com

Numbers displayed above are based on latest data collected.
For more information visit www.intechopen.com



Complex Digital Filter Designs for Audio Processing in Doppler Ultrasound System

Baba Tatsuro
Toshiba Medical Systems Corporation
Japan

1. Introduction

A medical Doppler ultrasound system has a spectrum display that indicates the blood flow direction, whether the blood flows forward or away from a probe. It also has Doppler audio outputs. In particular, the latter is a special process peculiar to the Doppler ultrasound system and separates the blood flow direction and outputs from the left and right speakers. Owing to this function, the existence of a blood flow is quickly detectable. When changing conventional analog signal-processing into digital signal-processing, we researched many processing systems of Doppler audio. First, target performances, such as a response time and direction separation, were set up, and six kinds of digital signal-processing systems were examined. Further, we investigated some new anti-aliasing processing systems unique to Doppler ultrasound system. We compared three kinds of anti-aliasing processing systems. Consequently, we clarified that a complex IIR (infinite impulse response) filter system has an excellent response and a low calculation load.

2. Outline of Doppler ultrasound system and conventional analog signal-processing

Recently, the diagnostic ultrasound system has been popular in many diagnostic fields, such as cardiac, abdomen, and so on. In Section 2.1, an example of diagnostic image and its principle are introduced. In Section 2.2, the phase shift system that is an example of representation of conventional analog signal-processing is introduced.

2.1 Outline of Doppler ultrasound system

An example of diagnostic image of a carotid artery is shown in Fig. 1. The upper is a tomogram image and bottom is a spectrum Doppler image. This image expresses the time change of the flow velocity in the PWD (Pulse Wave Doppler) range gate set up in the central of a blood vessel in a tomogram. A horizontal axis and a vertical axis are the flow velocities corresponding to Doppler shift frequency and time, respectively.

Signal processing of the ultrasound echo signal is shown in Fig. 2. An ultrasonic wave is transmitted for every cycle of PRF (pulse repetition frequency: f_s) in the transceiver processing part of Fig. 2(a), and a reflective echo is received. An ultrasonic beam is scanned in the transverse direction, and envelope detection of the received signal is carried out in the range direction. This scanning constitutes the tomogram image.

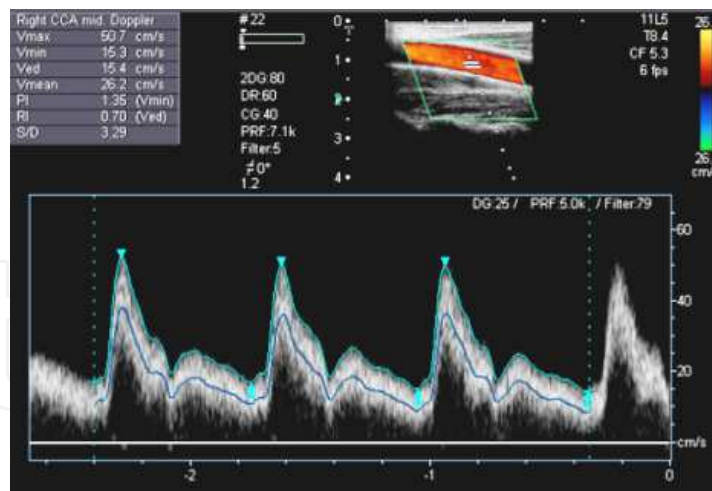


Fig. 1. Example of ultrasound diagnostic image of a carotid artery

Except for Doppler signal processing, as another method of blood-flow or tissue velocity detection, the cross-correlation method using the signal before quadrature-detection processing ($R(t)$ in Fig. 2(a)) has been also reported. However, the base-band signal ($L(t)$ in Fig. 2(a)) processing after quadrature-detection is the present mainstream, because of its narrow bandwidth and little processing load. All the direction separation systems examined this time are the IQ-signal processing after quadrature-detection. The received signal $R(t)$ in a range gate is denoted by a formula (1). Here, a reflective echo signal is assumed to be the amplitude A_i , Doppler shift angle-frequency ω_i , and phase ϕ_i .

$$R(t) = \sum_i A_i \cdot \exp(j \cdot (\omega_p + \omega_i) \cdot t + j \cdot \phi_i) \quad (1)$$

The mixer output $M(t)$ is denoted by a formula (2). Reference angle-frequency of a mixer is set to ω_p (same as probe Tx angle-frequency) here.

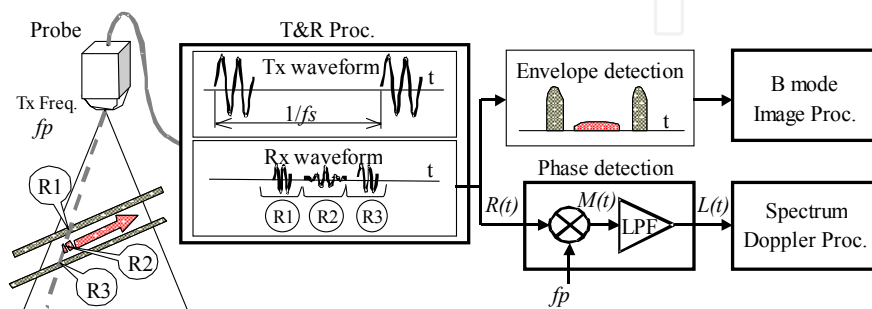
$$\begin{aligned} M(t) &= R(t) \cdot \exp(j \cdot \omega_p \cdot t) \\ &= \frac{1}{2} \sum_i A_i \cdot \exp(j \cdot (2 \cdot \omega_p + \omega_i) \cdot t + j \cdot \phi_i) + \frac{1}{2} \sum_i A_i \cdot \exp(j \cdot \omega_i \cdot t + j \cdot \phi_i) \end{aligned} \quad (2)$$

The LPF output $L(t)$, high frequency component is removed is denoted by a formula (3).

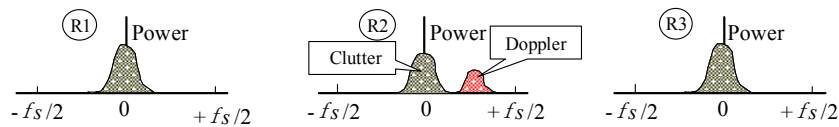
$$L(t) = \frac{1}{2} \sum_i A_i \cdot \exp(j \cdot \omega_i \cdot t + j \cdot \phi_i) \quad (3)$$

In Fig. 2(a) (R1), (R2), and (R3) show the position of the blood-vessel-wall upper part, the inside of a blood vessel, and the blood-vessel-wall lower part, respectively. Fig. 2(b) shows typical spectra of quadrature-detection output $L(t)$, when a range gate is set in each position. A vertical axis shows power and the horizontal axis shows frequency, respectively. Since the sampling is interlocked with PRF of transmission, the vertical axis has a frequency range of $\pm fs/2$. $L(t)$ is mainly constituted from the low frequency component caused by the clutter (strong echo from tissue) and middle to high frequency component caused by weak blood-

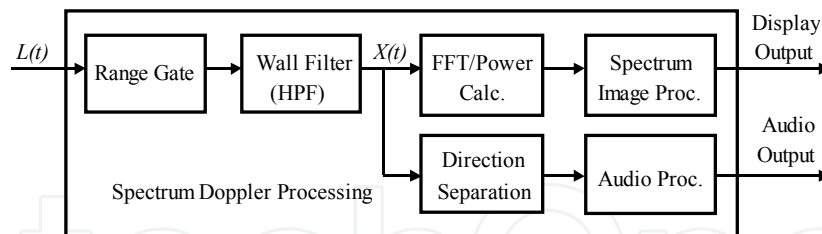
flow. Also inside of blood vessel, a blood vessel wall and a transmit-wavelength influence the blood-flow signal. Then, in order to prevent the saturation of the frequency analysis or the Doppler audio processing, a wall-filter is arranged in pre-processing of them. The wall-filter is HPF with high order cut-off property. The details of Spectrum Doppler signal processing are shown in Fig. 2(c). Range gate processing is the integration of $L(t)$ in the range direction in the range gate. Wall-filter processing removes a clutter component. The complex IQ-signal $x(t)$ after these processing is inputted into the spectrum Doppler display processing and the Doppler audio processing. The former displays the spectrum Doppler as a time-change image of a flow velocity. The latter separates the direction of Doppler signal, and outputs them as stereo sounds from a right-and-left speaker.



(a) The outline of signal-processing of ultrasound system



(b) Spectra of baseband IQ-signal



(c) Spectrum Doppler processing

Fig. 2. Doppler ultrasound signal-processing.

2.2 Conventional analog signal-processing

An analog phase-shift processing system that consists of all-pass filters has been used in the direction separation processing. The outline of it is shown in Fig. 3. This is a processing system that shifts the phase between the IQ-signals of 90 degree, and adds them or subtracts them. Since an all-pass filter has the characteristic that the phase reverses on cut-off frequency, this system shifts the phase in a target frequency range combining all-pass filter arrays. If it assumes that the input IQ-signal $x(t)$ has a frequency component of ω_d .

$$x(t) = \exp(j \cdot \omega_d \cdot t) \tag{4}$$

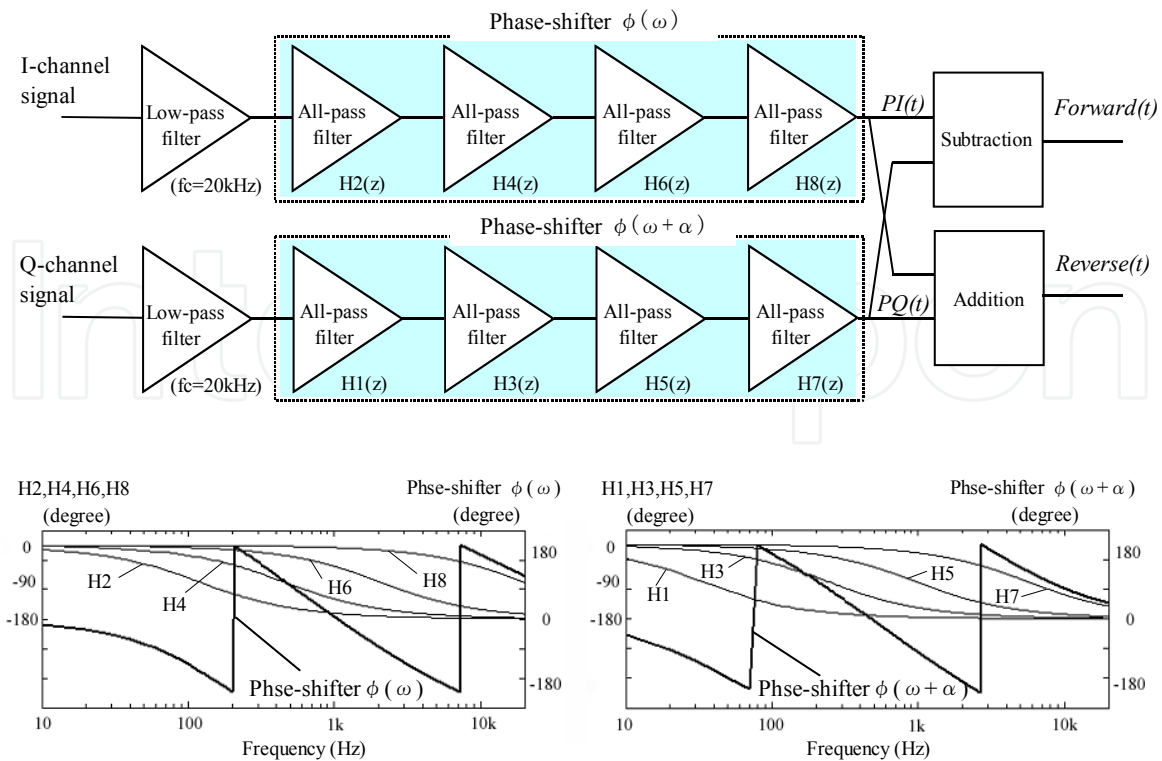


Fig. 3. Outline of analog direction separation system

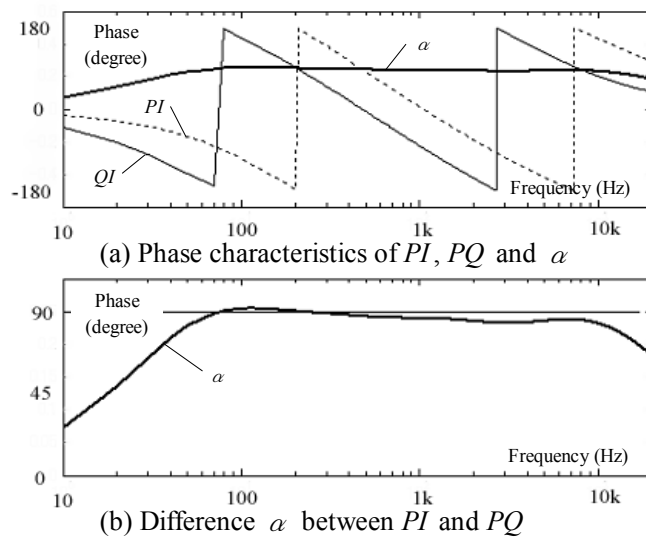


Fig. 4. Frequency characteristics of all-pass filters

In Fig. 4(b), the phase characteristics of I-channel and Q-channel are delayed as frequency becomes high. Here, the phase characteristics of I-channel and Q-channel are defined to be $\phi(\omega) + \alpha$ and $\phi(\omega)$, respectively. The output of I-channel and Q-channel are set to $PI(t)$ and $PQ(t)$.

$$PI(t) = \text{Re}[x(t) \cdot \exp(j \cdot (\phi(\omega) + \alpha))] = \text{sign}(\omega_d) \cdot \sin(\omega_d \cdot t + \phi(\omega)) \tag{5}$$

$$PQ(t) = \text{Im}[x(t) \cdot \exp(j \cdot (\phi(\omega)))] = -\sin(\omega_d \cdot t + \phi(\omega)) \quad (6)$$

Here, α is $-\pi/2$ when Doppler frequency ω_d is positive, and α is $+\pi/2$ when ω_d is negative. So $\text{sign}(\omega_d)$ means the polarity. The subtraction-output $Forward(t)$ and the addition-output $Reverse(t)$ are

$$Forward(t) = PI(t) + PQ(t) = (\text{sign}(\omega_d) + 1) \cdot \sin(\omega_d \cdot t + \phi(\omega)) \quad (7)$$

$$Reverse(t) = PI(t) - PQ(t) = (\text{sign}(\omega_d) - 1) \cdot \sin(\omega_d \cdot t + \phi(\omega)) \quad (8)$$

From the formulas (7) and (8), when ω_d is positive, only the $Forward(t)$ serves as a non-zero output. And when ω_d is negative, only the $Reverse(t)$ serves as a non-zero output. Thus, IQ-signals are separable into positive-component and negative-component. Comparison of direction separation performance is shown in Fig. 5. The frequency-characteristic in the velocity range 4kHz (-2kHz to +2kHz) that is well used in diagnosis of the cardiac or abdomen is shown. A solid line shows the positive-component ($Forward$) and a dashed line shows the negative-component ($Reverse$). The direction separation performance of the phase-shift system (conventional analog system) is shown in Fig. 5(a), and the direction separation performance of the complex IIR filter system (digital system referenced in section 3.2) is shown in Fig. 5(b).

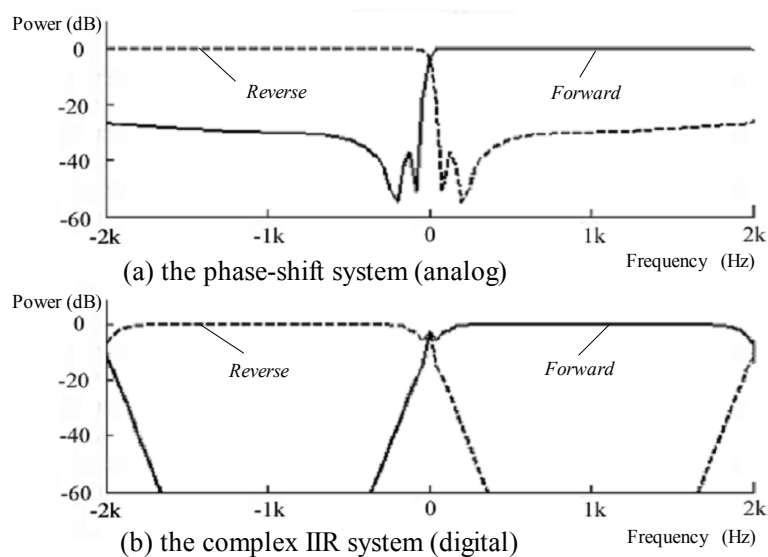


Fig. 5. Direction separation performance

In Fig. 5, a filter-order to which hardware size becomes same is set up. In the complex IIR filter system, sufficient separation performance (more than 30 dB) is got except for near a low frequency and near the Nyquist frequency. On the one hand a ringing has occurred by the phase shift system, there is little degradation near the Nyquist frequency. Although the direction separation performance near a low frequency and near the Nyquist frequency can improve if the filter-order is raised in the complex IIR filter system, the processing load becomes large. It is although the ringing will decrease if range of the phase-shift system is divided finely, processing load becomes large similarly.

3. Comparison of six kinds of Doppler audio processing

The digitization of Doppler ultrasound system had progressed in recent years, and the digital signal processing using DSP etc. can realize complex processing easily from the conventional analog-circuit. We made the target performances of the direction separating process of digital Doppler audio, and evaluated six kinds of digital-signal processing ideas that were pre-existing or were newly devised.

3.1 Design of a target specification

For the digitization, the target performance is investigated and taken up to Table 1.

item	target
1. time-delay	bellow 20ms (PRF 4kHz)
2. direction separation	above 30dB
3. frequency characterization	$f_s/128$ to $63 \cdot f_s/128$ (both direction) flat as possible
4. frequency resolution	$f_s/100$
5. calculation volume	light as possible

Table 1. Requirement specification of Doppler audio direction separation

Time-delay:

A user usually sets up the Doppler range gate on a tomogram, moves it, and performs blood flow diagnosis with the Doppler ultrasound system. In searching for a small blood vessel, the Doppler audio is effective, because its response is faster than that of the spectrum image. This is because a tomogram set with the Doppler audio delays the outputs of about 20 ms, compared with the spectrum image that has a typical delay of about 40 ms. The time delay of tomogram processing is a few cycle of one frame (13.3 - 16.7 ms). In the Doppler signal processing system, it has a total processing delay of 10 ms by quadrature-detection and HPF processing, except for the Doppler processing part. Therefore, to make the tomogram and audio agree, a time delay of 3.3 - 6.7 ms is required at the Doppler signal processing part. However, because the direction separation process, which is the main factor of the Doppler signal processing part delay, requires a number of series samplings for processing, a target time delay is theoretically difficult to achieve. Therefore, the target time delay was set to be 20 ms or smaller, so that the target delay time required for the direction separation process to store the Doppler audio is about one frame cycle at maximum in a tomogram.

Direction separation:

It has been reported that human's direction distinction requires a right-and-left signal difference of 15 to 20 dB or lager. In an actual Doppler ultrasound system, considering that the Doppler signal has a broad band, that the angle between the right-and-left speakers is small, and that blood flow velocity changes with time, a larger signal difference is required. The target performance of direction separation was set to be 30 dB or higher at observation frequency.

Frequency characteristic:

A signal processing frequency range is the range f_s from negative-side Nyquist frequency to positive-side Nyquist frequency, where f_s is input IQ-signal sampling frequency. We made the frequency characteristic flat in the region of $\pm f_s / 128$ to $\pm 63 \cdot f_s / 128$ range.

Frequency resolution:

Since spectrum image signal processing involves 256-point FFT, an acceptable frequency (velocity) resolution is obtained. However, when the frequency resolution of the Doppler audio is unacceptable, similar to that of a small-pitch Doppler image, we set the target resolution to be $f_s/100$. The frequency range is determined from sample frequency. However, the frequency resolution is proportional to the reciprocal of observation time. For example, in FFT, it is equivalent to the main lobe width of the sampling function determined from observation time width and the window function.

Calculation load:

Although operation load is dependent on the hardware-architecture, such as DSP, ASIC, and FPGA, lighter load is more advantageous to cost, size, and power consumption in common.

3.2 Six kinds of digital signal-processing ideas

Six kinds of digital signal-processing systems that were pre-existing or newly devised are examined. They are shown in Fig. 6.

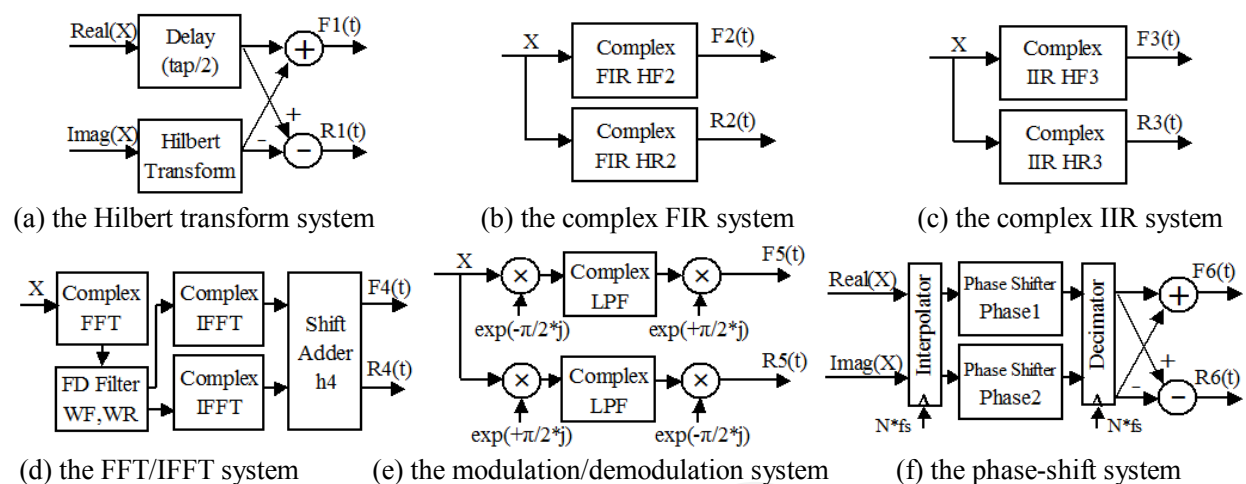


Fig. 6. Six kinds of digital signal-processing systems

Hilbert transform system:

The delay of (filter tap length)/2 is given to I-channel of IQ-signals. It and the Hilbert transform output of Q-signal are subtracted or added. The direction separated signals are calculated by formulas (9) and (10). Here a convolution is indicated \otimes . The tap number is set to 128 in the estimation of the calculation load shown in Table 3.

$$F1(n) = \text{Re}(X(n - n_{\text{tap}} / 2)) + \text{Im}(X(n) \otimes h1(n_{\text{tap}})) \tag{9}$$

$$R1(n) = -\text{Re}(X(n - n_{\text{tap}} / 2)) + \text{Im}(X(n) \otimes h1(n_{\text{tap}})) \tag{10}$$

The coefficient $h1$ of Hilbert transform is given by a formula (11).

$$h1(n) = \begin{cases} \frac{2}{\pi} \cdot \frac{\sin^2(\pi \cdot n / 2)}{n} & (n \neq 0) \\ 0 & (n = 0) \end{cases} \quad (11)$$

Complex FIR system:

There is a report of the Doppler audio separation processing using a complex FIR filter. However, since there is no description about a filter coefficient, we designed in a frequency domain and transformed into FIR coefficient in time domain using inverse Fourier transform. The output of complex FIR system is denoted by formulas (12) and (13). In the estimation of Table 3, the 128-tap coefficient sequence with the pass band of $\pm fs / 128$ to $\pm 63 \cdot fs / 128$ is used.

$$F2(n) = X(n) \otimes HF2(ntap) \quad (12)$$

$$R2(n) = X(n) \otimes HR2(ntap) \quad (13)$$

Complex IIR system:

Based on the shift theory of Fourier transform, frequency shift is applied to z operators. A real-LPF transfer function is changed into the positive-BPF and the negative-BPF. The complex IIR transfer functions become a formulas (14) and (15).

$$F3(z) = HF3(z) \cdot X(z) \quad (14)$$

$$R3(z) = HR3(z) \cdot X(z) \quad (15)$$

When the transfer function of real LPF is set to $RLPF(z)$, transfer functions of $HF3(z')$ and $HR3(z'')$ are calculated by transformed operators. In the estimation of Table 3, the filter with the 8th order Butterworth type is used.

$$HF3(z) = RLPF3(z') \quad \text{where} \quad z' = -j \cdot z \quad (16)$$

$$HR3(z) = RLPF3(z'') \quad \text{where} \quad z'' = j \cdot z \quad (17)$$

FFT/IFFT system:

The IQ-signal is separated by the positive-filter and negative-filter in a frequency domain. Next, the separated spectra are returned to waveforms in time domain by inverse-FFT. There is a report of this system aiming at the Doppler noise rejection. For the continuous output after inverse-FFT, a shift addition of the time waveform is carried out in time domain. The outputs of this system can be denoted by formulas (18) and (19). In estimation of Table 3, FFT/IFFT point number is set to 128, and used the frequency filter of $\pm fs / 128$ to $\pm 63 \cdot fs / 128$ for separation. Moreover, Hamming window ($h4$) is applied, and 32 time-series are shift-added.

$$F4(n) = \text{Re}\left(\text{IFFT}\left(\text{WF}(\omega) \cdot \text{FFT}\left(X(n)\right)\right)\right) \cdot h4(n) \quad (18)$$

$$R4(n) = \text{Re}\left(\text{IFFT}\left(WR(\omega) \cdot \text{FFT}\left(X(n)\right)\right)\right) \cdot h4(n) \quad (19)$$

Modulation/demodulation system:

IQ signal is modulated and frequency is shifted $+fs/4$ and $-fs/4$. The positive-component (0 to $+fs/2$) and negative-component ($-fs/2$ to 0) are extracted by LPF. The $+fs/4$ shift and the $-fs/4$ shift are returned by demodulation. The direction separation outputs are calculated by formulas (20) and (21). The example of Table 3 is referred to the prior art. The 128-tap FIR low-pass filter, which has 63/128 cut-off, is used.

$$F5(n) = \left(\left(X(n) \cdot \exp\left(-\frac{\pi}{2} \cdot j \cdot n\right) \right) \otimes \text{CLPF}(ntap) \right) \cdot \exp\left(+\frac{\pi}{2} \cdot j \cdot n\right) \quad (20)$$

$$R5(n) = \left(\left(X(n) \cdot \exp\left(+\frac{\pi}{2} \cdot j \cdot n\right) \right) \otimes \text{CLPF}(ntap) \right) \cdot \exp\left(-\frac{\pi}{2} \cdot j \cdot n\right) \quad (21)$$

Phase-shift system:

There are two sets of phase-shifter with the transfer characteristic that makes relative phase difference of IQ-signal 90 degree. The addition-and-subtraction of these outputs is used. The direction separation outputs are calculated by formulas (22) and (23).

$$F6(z) = \text{Re}(X(z)) \cdot \text{Phase1}(z) + \text{Im}(X(z)) \cdot \text{Phase2}(z) \quad (22)$$

$$R6(z) = -\text{Re}(X(z)) \cdot \text{Phase1}(z) + \text{Im}(X(z)) \cdot \text{Phase2}(z) \quad (23)$$

The two sets of phase-shifter are the cascade connection of second-order all-pass filter arrays. They are denoted by formulas (24) and (25) as a *Phase1* (*z*) and a *Phase2* (*z*). In the estimation of Table 3, the cascade connections of four steps of all-pass filters are used. Moreover, in order to improve the performance near the Nyquist frequency, an interpolator and a decimator are added before and after phase-shifter. Table 3 is calculated in $N=4$, and the FIR filter of $2N$ tap is used as an interpolator.

$$\text{Phase1}(z) = \prod_{k=1}^n \frac{z^{-1} - a_k}{1 - a_k \cdot z^{-1}} \quad (24)$$

$$\text{Phase2}(z) = \prod_{k=1}^n \frac{z^{-1} - b_k}{1 - b_k \cdot z^{-1}} \quad (25)$$

Above six kinds of signal-processing algorithms are confirmed by the simulation. The chirp-waveform that frequency and a direction are changed is used as an input. The result of a simulation is shown in Fig. 7. Fig. 7(a) is an input signal and the sign of frequency has inverted near 200ck (equivalent to the time shown in the Fig. 7 broken line). A solid line is I-signal and a dotted line is Q-signal. Figures 7(b) to (g) are output waveforms of each signal-processing system. A solid line is a positive-output (forward) of the Doppler audio, and a dotted line is a negative-output (reverse) of the Doppler audio. Amplitude of positive-output becomes large on the right-hand side of a broken line, and it becomes small on the

left-hand side of the broken line. Amplitude of negative-output becomes small on the right-hand side of a broken line, and it becomes large on the left-hand side of the broken line. This result shows that each system works correctly. Moreover, it shows that the waveform and response time at the turning point of sign (near the DC) have a difference among the systems. As these causes, performance differences, such as the response characteristic and delay time, can be considered.

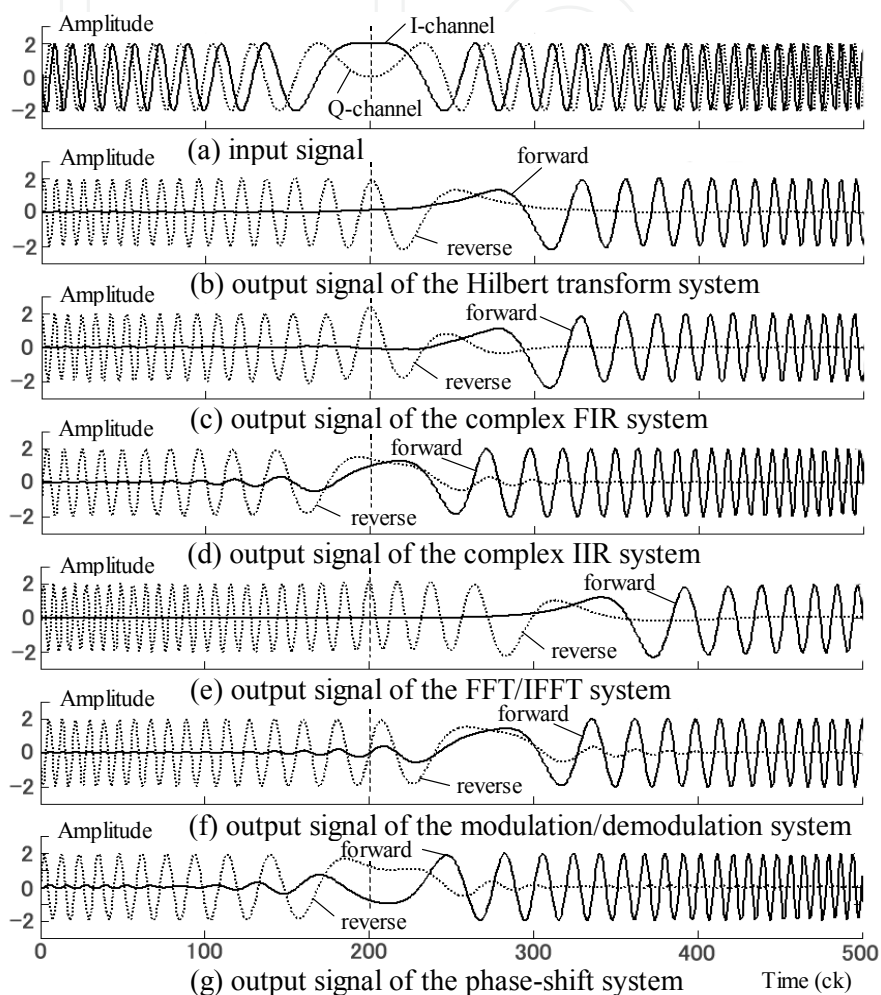


Fig. 7. Chirp wave responses

3.3 Comparison of time-delay and calculation load

The response is important for blood vessel detection, and the time-delay estimates it. The simulation result of the time-delay is shown in Fig. 8. They are response waveforms of the sinusoidal-waveform that changes discontinuously. Solid line and dotted line are I-signal and Q-signal in Fig. 8(a). Amplitude and frequency are changing near the 50ck. The solid lines of Fig. 8(b) and Fig. 8(c) are positive-output waveforms, and dotted lines are negative-output waveforms. The output waveform of the complex FIR system of Fig. 8 (b) changed from a turning point of the input shown with the dashed line after 64ck (time shown with the chain line among Fig. 8(b)), and is stable gradually. The output waveform of the complex IIR system of Fig. 8(c) is stable from the turning point after 8ck (time shown with the chain line among Fig. 8(c)).

The comparison of time-delay is shown in Table 2. Frequency resolution is adjusted by parameter of each system in accordance with the target performance of Table 1. Since the signal-processing inputs are sampled by f_s , time-delay will become large if f_s becomes low. Table 2 is calculated by $f_s=4\text{kHz}$ condition. Incidentally by $f_s=1\text{kHz}$, time-delay increases 4 times. The time-delay caused by operation is assumed zero, and estimated only the delay caused by sampling simply. Moreover, the influence of the transient response of the complex IIR system and the phase-shift system is not taking into consideration here.

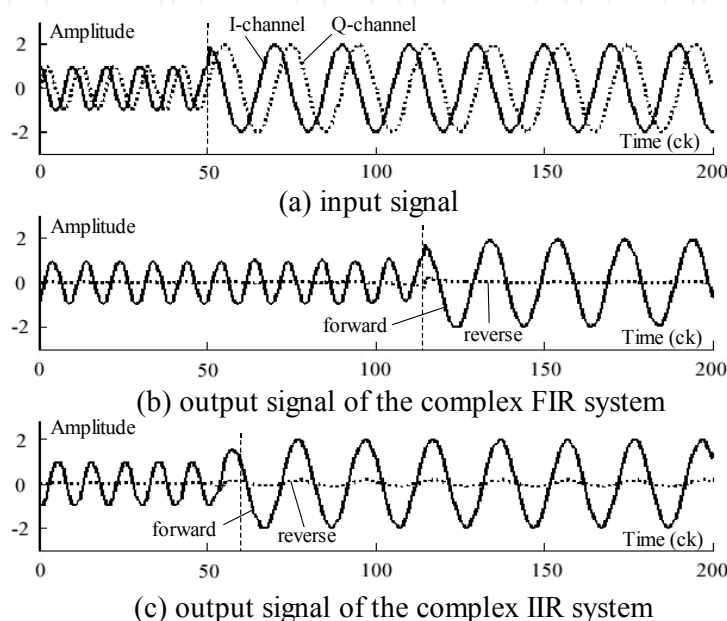


Fig. 8. Comparison of response between complex FIR method and complex IIR method

method	estimation	time-delay (ms)
Hilbert transform	tap/f_s	32 ($tap=128$)
Complex FIR	tap/f_s	32 ($tap=128$)
Complex IIR	$order/f_s$ (*1)	2 ($order=8$)
FFT/IFFT	$1.5*N/f_s$ (*2)	48 ($N=128$)
Moduration/Demoduration	tap/f_s	32 ($tap=128$)
Phase shift	$\max(2,order/N)/f_s$ (*1)	1 ($order=4, N=1$)

Estimated at $f_s=4\text{kHz}$, (*1) not including transient response, (*2) IFFT shift addition pitch is $N/4$

Table 2. Comparison of time-delay

As calculation load depends on the hardware architecture, the multiplication and addition times per 1 second (floating point single precision) is used for this estimation. Moreover, the complex-multiplication is considered as 4 times, and complex-addition is considered as twice. The overhead of the processing which requires a lot of memory buffers is assumed to be 20%. The other overhead is assumed to be 10%. The calculation elements, estimation formula and calculation load for each signal-processing systems are shown in Table 3. Incidentally, at $f_s=52\text{ kHz}$ (maximum PRF in actual system), calculation load increases 13 times. The result of Table 2 and Table 3 shows that the complex IIR system and the phase-

shift system are filling the target performance of time-delay. It turns out that calculation load is light in order of the phase-shift system, the complex IIR system, and the Hilbert transform system.

method	calculation component	estimation equation	load (MFLOPS)
Hilbert transform	R-add: $(tap+1)*fs$, R-mul: $tap*fs$ Ovh: 20%	$fs*(2*tap+1)*1.2$	1.26 ($tap=128$)
complex FIR	C-add: $(tap-1)*2+fs$, C-mul: $tap*2*fs$ Ovh: 10%	$fs*(12*tap-4)*1.1$	6.74 ($tap=128$)
complex IIR	C-add: $order*4*fs$, C-mul: $order*4*fs$ Ovh: 10%	$fs*(24*order)*1.1$	0.84 ($order=8$)
FFT/IFFT	C-add: $N*r*3$, C-mul: $(N*r/2)*3$ Ovh: 20%, R-mul: $N*4$	$12*N*r*1.2*(fs*4/N)$ (FFT shift addition, $N/4$ shift)	1.61 ($N=128, r=7$)
modulation/demodulation	C-add: $(tap-1)*2*fs$ C-mul: $(tap+2)*2*fs$, Ovh: 20%	$fs*(12*tap-12)*1.2$	7.32 ($tap=128$)
Phase-shift	R-add: $[2*N*(2*N+2*order)+2]*fs$ R-mul: $4*N*(N+order)*fs$, Ovh: 20%	$fs*[4*N*(N+order)+2*(N-1)]*1.2$	0.64 ($order=4, N=4$)

R-add: real addition, R-mul: real multiplication, Ovh: over head, C-add: complex addition, C-mul: complex multiplication, Calculation load is estimated at $fs=4kHz$

Table 3. Comparison of calculation load

3.4 Comparison of a frequency characteristic and direction separation

Frequency characteristic and direction separation performance are largely dependent on the filter property that are related to time-delay and calculation load. If the number of filter taps of FIR and the filter order of IIR are reduced, time-delay and calculation load will decrease. But these become the trade-off of frequency resolution and frequency characteristic. The Hilbert transform system frequency characteristic when changing the number of taps is shown in Fig. 9. The frequency characteristic near the Nyquist and near the DC has deteriorated, when the number of taps is short. This is the same also about the taps of the complex FIR system, the modulation/demodulation system and the FFT point number of the FFT / IFFT system.

In order to compare the direction separation performance, the frequency characteristic simulation is performed. The frequency characteristics of positive-component (solid line: forward) and negative-component (dashed line: reverse) are shown in Fig. 10. The target performance of direction separation is filled except for the phase shift system. The stop-band property near the low frequency and near the Nyquist frequency is good in the Hilbert transform system, the complex FIR system, and the FFT/IFFT system. Exclude near the DC and near the Nyquist frequency, a sufficient separation performance (not less than 30 dB) and frequency characteristic are acquired by the complex IIR system and the modulation/demodulation system. The phase-shift system has generally insufficient

separation performance. The separation performance is deteriorated especially near the Nyquist frequency.

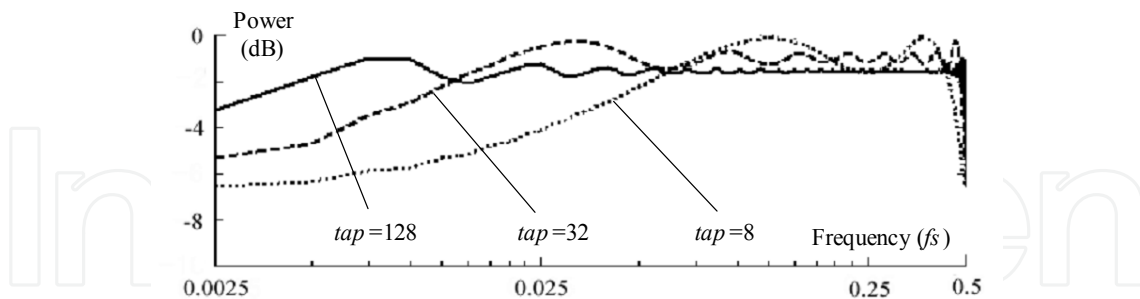


Fig. 9. Example of frequency response: the Hilbert transform system

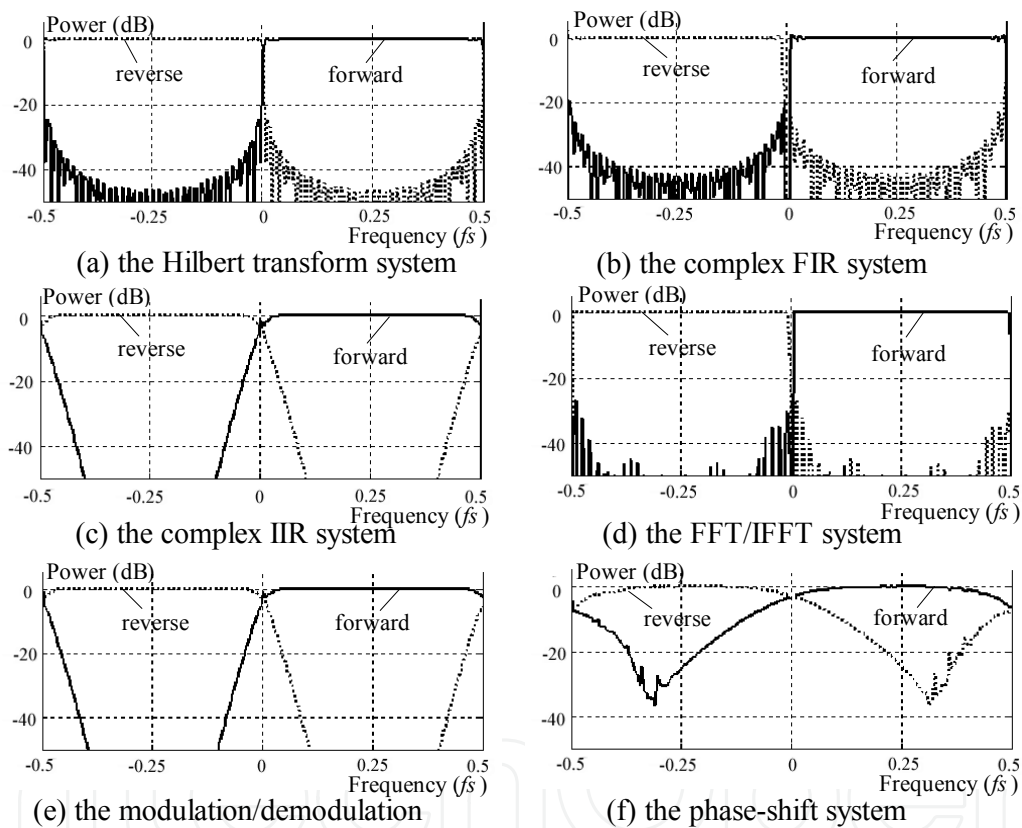


Fig. 10. Frequency characterization and direction separation performance

3.5 Conclusion

We made the target performances of the direction separating process of digital Doppler audio, and evaluated six kinds of digital-signal-processing ideas that were pre-existing or were newly devised. The performances of each processing were evaluated by comparing many responses such as chirp or step and so on. The results are following.

1. The complex IIR system and the phase-shift system are filling the target performance of response time.
2. The target performance of direction separation is filled except for the phase-shift system.

3. All the systems fill the frequency characteristic. However, the frequency characteristics near the DC and near the Nyquist region are dependent on the filter characteristics of each processing system.

4. Signal processing for Doppler audio anti-aliasing

The direction separation system of the foregoing section is developed further, and the Doppler audio technology exceeding the Nyquist frequency is examined. Some direction-separation systems for a Doppler audio that is interlocked with the baseline-shift of a spectrum image are investigated. First, section 4.1 explains a problem peculiar to the Doppler audio corresponding to the Doppler display processing. In section 4.2 we defined the target performance of anti-aliasing Doppler audio processing selected three kinds of signal-processing systems. In section 4.3 the various systems of the modulation/demodulation system, the FFT/IFFT system and the complex IIR Filter system are explained. Next, in section 4.4 the signal-processing algorithms are compared with the target performances. It was confirmed that the complex IIR band-pass filter system has an excellent response and a low calculation load. Finally, in section 4.5 using the blood-flow data collected from Doppler phantom, we performed functional and performance analyses by simulation shown in Fig. 22.

4.1 Anti-aliasing display and conventional problem

The Doppler ultrasound system extracts the blood flow component used in the quadrature-detection of the Doppler signal from the blood (mainly an erythrocyte), which moves inside a blood vessel, and removes a reflective signal from tissue, such as a blood vessel wall with a high-pass filter, and transforms the Doppler component into an image and sound. The Doppler ultrasound system is shown in Fig. 11. The signal obtained after HPF processing is divided into two lines. Spectrum image processing generates a Doppler signal as a spectrum time change image corresponding to blood velocity, and Doppler audio processing outputs direction separation signals as stereo sound from the right-and-left speakers.

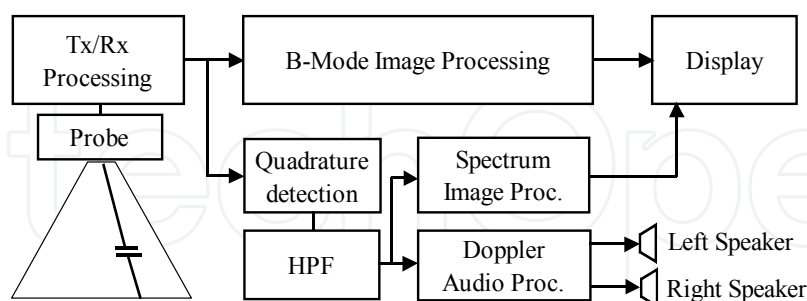


Fig. 11. Doppler ultrasound system.

Because the Doppler signal contains phase information, the signal includes both positive-side (forward) and negative-side (reverse) frequency components. If sampling frequency is set to be f_s , the detection of a Doppler frequency component corresponding to the frequency range of $-f_s/2$ to $+f_s/2$ is possible. A spectrum image is shown in Fig. 12. The horizontal axis corresponds to time. The vertical axis corresponds to the velocity derived from Doppler shift frequency, and luminosity corresponds to the spectrum intensity of each time. Since a spectrum image is a power spectrum generated by complex FFT processing, it has the

frequency range of $-fs/2$ to $+fs/2$ on the baseline (0Hz) shown in Fig. 12(a). At the time (A) in Fig. 12, the frequency of the spectrum exceeds $+fs/2$ and aliasing is induced. The Doppler ultrasound system has an anti-aliasing display function (BLS: baseline-shift) that shifts a baseline to a negative side, as shown in Fig. 12(b), and expands a positive velocity range seemingly. Thus we can measure the peak velocity of blood flow easily. The power spectrum at the zero baseline-shift is shown in Fig. 13(a). The spectrum image at the $-0.25 \cdot fs$ baseline-shift and the power spectrum corresponding to the time (A) in Fig. 12 are shown in Fig. 13(b). In the spectrum image, a baseline-shift is easily realized by changing the frequency read-out operation of the spectrum after FFT processing. However, since there is no baseline-shift function in the Doppler audio, a baseline-shift is not realized in spectrum imaging and Doppler audio processing. For example, although a negative-component is lost in the spectrum image shown in Fig. 13(b), since Doppler sound is still in the state shown in Fig. 13(a), it displays a negative-output and does not correspond to the Doppler image.

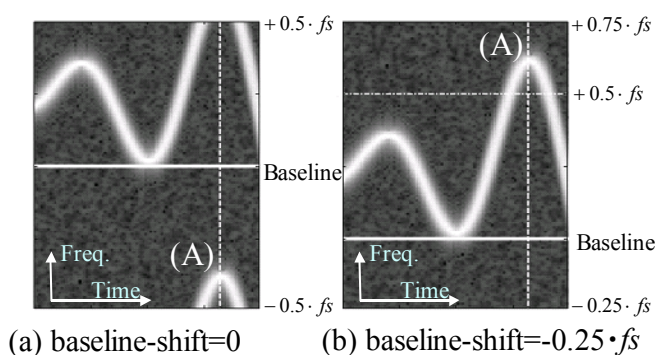


Fig. 12. Spectrum Doppler image

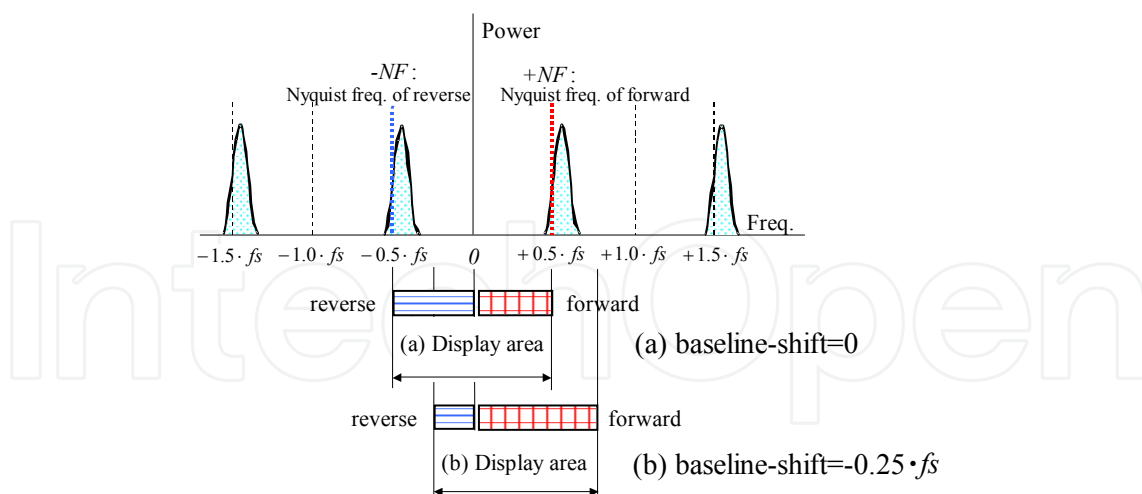


Fig. 13. Spectrum display area and baseline shift.

4.2 Anti-aliasing processing of Doppler audio and its target performance

To solve the problem of the spectrum image and Doppler audio not working together, we examined the signal processing system of the Doppler audio to determine the possible type of baseline-shift. On the other hand, since IQ-signals after quadrature-detection had little merit at a small operation load in narrow-band processing, we examined a realization

method based on the IQ-signals. The Hilbert transform, complex FIR filter, phase-shift, complex IIR filter, FFT/IFFT and modulation/demodulation systems also indicated that the direction separation system of the Doppler audio does not allow a baseline-shift. Among these systems, the Hilbert transform and phase-shift systems enable direction separation by addition and subtraction between signals with a 180-degree phase-difference. Since an input IQ-signal has a 90-degree phase difference, these systems give a phase-difference of 90 degree between channels with a filter. Since the phase-difference of an IQ-signal stops being 90 degree when sampling frequency is doubled as a countermeasure, in the Hilbert transform and phase-shift systems, which make the phase-difference between channels a simple 90 degree, direction separation is difficult. Moreover, the complex FIR filter system involves the same pre-processing step as that in the complex IIR filter system, and anti-alias processing becomes possible. However, since the length of a FIR coefficient sequence doubles, the operation load increases. On the other hand, the FFT/IFFT system can reduce the operation load by diverting the FFT output of spectrum Doppler imaging processing. When the FFT output is diverted, the returning anti-alias processing can be performed only by inverse-FFT and shift-addition. The modulation/demodulation and the complex IIR filter systems mainly involve the multiplication of modulation/demodulation and IIR filter processing. Thus, their calculation processing is easy, and the increase in calculation load by anti-aliasing processing is small. As mentioned above, from the viewpoints of calculation load reduction and anti-alias processing feasibility, we chose and examined the following three systems: the modulation/demodulation, the FFT/IFFT, and the complex IIR systems. When evaluating these systems, we showed the same target performance required as that of the Doppler ultrasound system in Table 4. The items 1 to 4 (time-delay, direction separation, frequency characteristic, frequency resolution) are same as table 1.

item	target
1. time-delay	bellow 20ms ($f_s=4\text{KHz}$)
2. direction separation	above 30dB
3. frequency characterization	$-f_s/128$ to $-127*f_s/128$, $f_s/128$ to $127*f_s/128$ flat as possible
4. frequency resolution	$f_s/100$
5. baseline-shift range	$-f_s/2$ to $+f_s/2$ (-0.5 to 0.5)

Table 4. Target specification of Doppler audio processing.

baseline-shift	-0.5	-0.25	0	0.25	0.5
<i>FB</i> : band-width of forward	4/8	3/8	2/8	1/8	0
<i>FBC</i> : center freq. of forward	4/16	3/16	2/16	1/16	0
<i>RB</i> : band-width of reverse	0	1/8	2/8	3/8	4/8
<i>RBC</i> : center freq. of reverse	0	-1/16	-2/16	-3/16	-4/16

Notes: Baseline shift, *FB*, *FBC*, *RB* and *RBC* are normalized by f_s .

Table 5. Frequency shift and bandwidth table of baseline-shift

Baseline-shift range:

The baseline-shift range is considered to be $-0.5*f_s$ to $+0.5*f_s$ to enable range expansion on the positive and negative sides to twice the Nyquist frequency range. The ranges of both

sides correspond to the baseline-shift shown in Table 5. FB and RB indicate the bandwidths on the positive (forward) and negative (reverse) sides, whereas FBC and RBC , the center frequencies on the same sides, respectively. These are normalized using f_s . Although five stages were used from the baseline shift range of -0.5 to $+0.5$ in this example, a small setup is possible with the actual Doppler ultrasound system.

4.3 Three kinds of digital signal-processing ideas

4.3.1 The modulation/demodulation system

The block diagram of the modulation/demodulation system is shown in Fig. 14. The IQ-signal is modulated with two sets of quadrature modulators. Thereby, the frequency of the signal induces a $+FBC$ shift on the positive-side and a $-RCB$ shift on the negative-side. Next, Nyquist frequency is doubled by zero insertion, and applying band limitations on the positive and negative sides demodulates signals. The input signal (equivalent to (A) in Fig. 12) with the aliasing spectrum in Fig. 15(a) is modulated, and the spectra indicating the $+FBC$, and $-RCB$ shifts of the frequency of the signal are shown in Figures 15(b) and 15(c), respectively. A positive-side component and a negative-side component are extracted by carrying out a baseline-shift and applying a band limitation using the bandwidths of $\pm FB$ and $\pm RB$ in the passage regions of $LPF1(z)$ and $LPF2(z)$. The spectra of the $LPF1(z)$ and $LPF2(z)$ outputs are shown in Figures 15(d) and 15(e). Since sampling frequency has doubled after an LPF output, the direction separations on the positive and negative sides that shift the frequencies of $-FBC/2$ and $+RCB/2$ by demodulation, and are denoted by $BPF1(z)$ and $BPF2(z)$ in Fig. 15(f) are realizable. Although the spectrum in Fig. 15 (equivalent to the aliasing (A) in Fig. 12) is outputted to the negative side for the Nyquist frequency $f_s/2$, it can extract the positive-side component beyond the Nyquist frequency in Fig. 15(f). The operation was changed and performed in the calculation example shown in Table 7. For response improvement, we did not use a FIR filter for LPF but the 8th IIR filter with an equivalent performance.

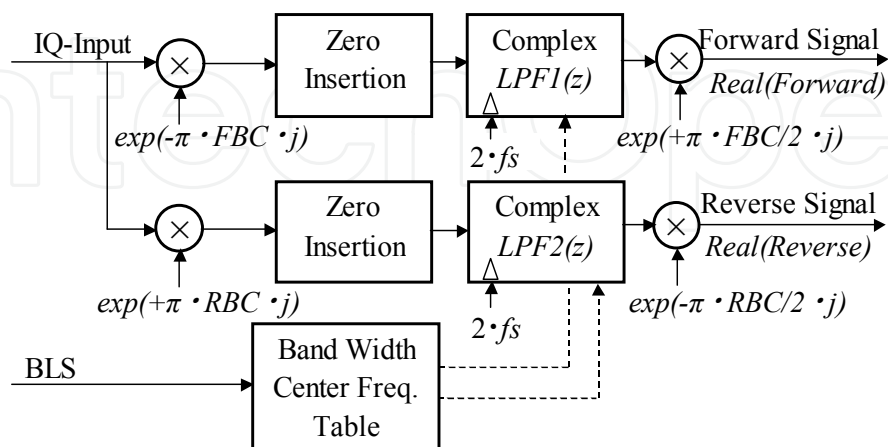


Fig. 14. Block diagram of the modulation/demodulation system

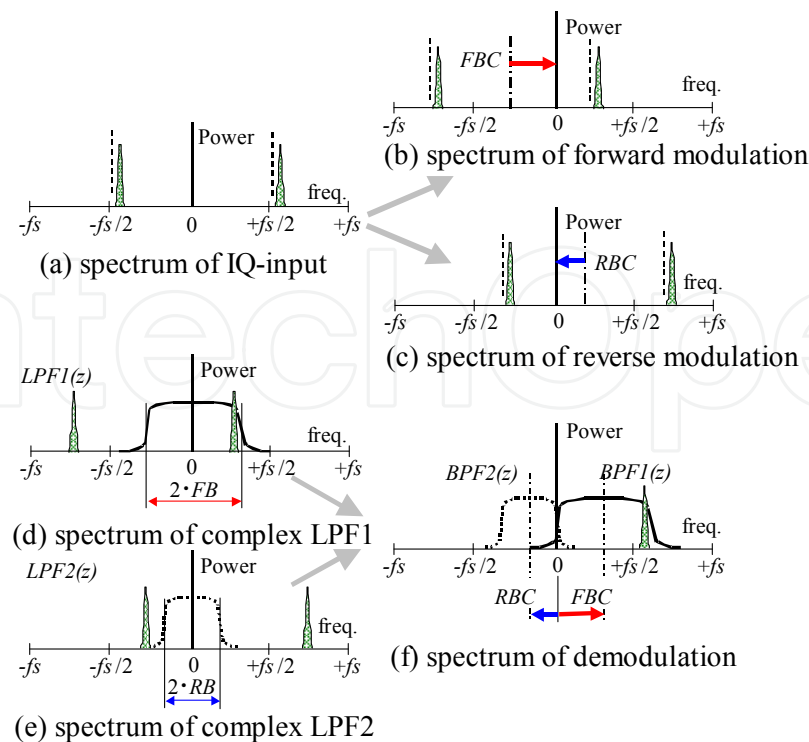


Fig. 15. Frequency design of the modulation/demodulation system

4.3.2 The FFT/IFFT system

The block diagram of the FFT/IFFT system is shown in Fig. 16. Two sets of filters corresponding to the baseline-shift separate the IQ-signal after FFT processing. These filters are realized by applying $WF(\omega)$ and $WR(\omega)$ with the characteristics of FB , RB , FBC , and RBC shown in Table 6. Next, the separated spectra are returned to the time domain signals by inverse-FFT. Since the frequency range expands on the basis of the baseline-shift, we perform twice-point inverse-FFT. Further shift in time waveform after inverse-FFT is carried out, and a continuous output is obtained. The power spectrum of the IQ-signal after FFT is shown in Fig. 17(a). When the baseline-shift is terminated, the spectrum in the figure (equivalent to the aliasing (A) in Fig. 12) is observed on the negative-side. However, by operating the read-out address of FFT, the positive display range is expanded and observed on the positive-side. Similarly, by carrying out inverse-FFT processing with $WF(\omega)$ and $WR(\omega)$ with a frequency twice that of sampling ($2 \cdot fs$), the frequency range of the Doppler

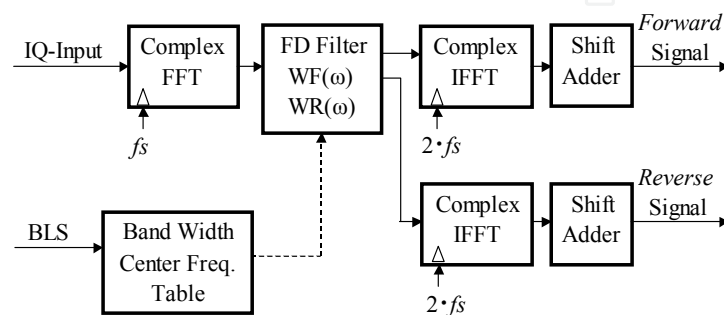


Fig. 16. Block diagram of the FFT/IFFT system

audio is expanded, and the positive-side component in Fig. 17 (b) and the negative-side component in Fig. 17 (c) are obtained. In the calculation example shown in Table 7, we perform 128-point FFT and 256-point inverse-FFT. Moreover, we perform the shift-addition of 32 time series data to which the Hamming window is applied after inverse-FFT.

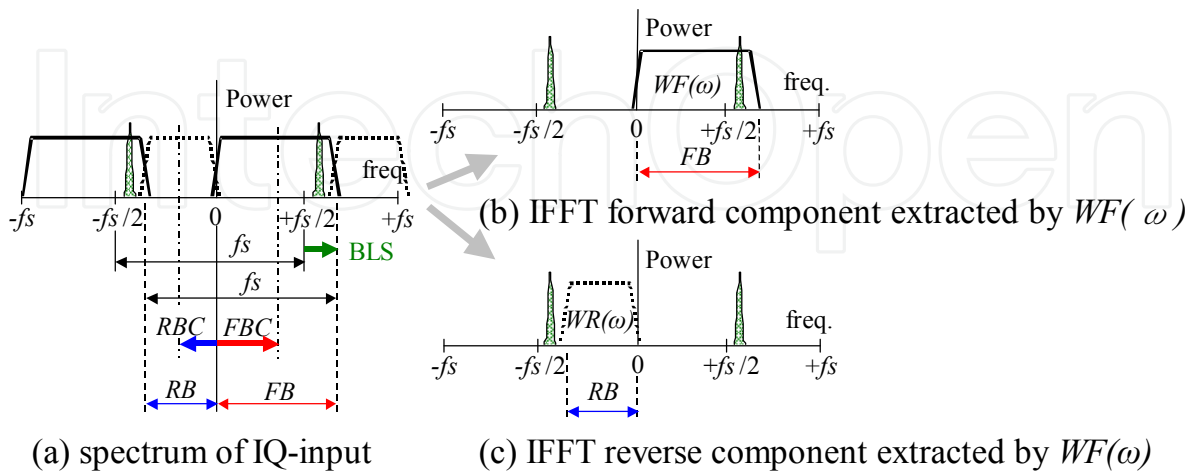


Fig. 17. Frequency design of the FFT/IFFT system

4.3.3 The complex IIR filter system

The signal processing block diagram of the complex IIR filter system is shown in Fig. 18. Zero insertion is carried out with a pre-treatment, and Nyquist frequency is increased. Next, two complex band-pass filters separate both components directly. The frequency characteristics of the transfer functions $H_f(z)$ and $H_r(z)$ with the bandwidths of FB and RB (one side bandwidth) for LPF are shown in Figures 19(a) and 19(b). On the basis of the Fourier transform shift theory, the frequency shifts (FBC and RBC) are applied to z operators, and a transfer function of LPF changes to the positive-side and a negative-side band-pass filters. Operator z is transformed to $z' = z \cdot \exp(-j \cdot FBC)$ and $z'' = z \cdot \exp(-j \cdot RBC)$. The frequency characteristics of the complex band-pass filters $H_f(z')$ and $H_r(z'')$ enable the $+FBC$ and $-RBC$ frequency shifts are shown in Fig. 19(c). In the calculation example shown in Table 7, we use the 8th Butterworth filter by considering the response of direction separation.

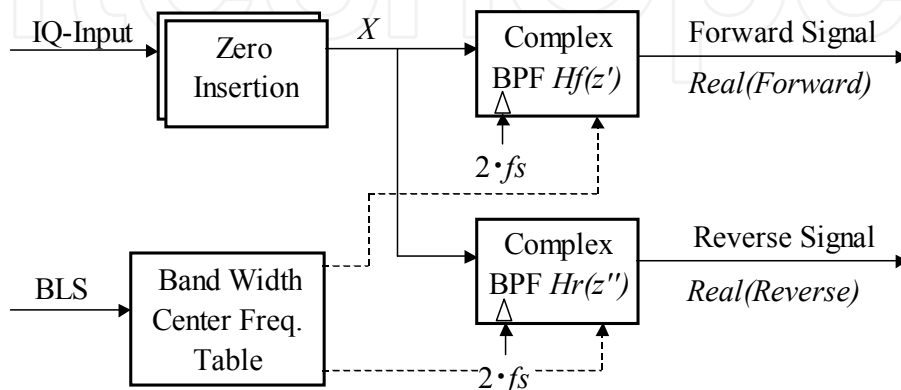


Fig. 18. Block diagram of the complex IIR filter system

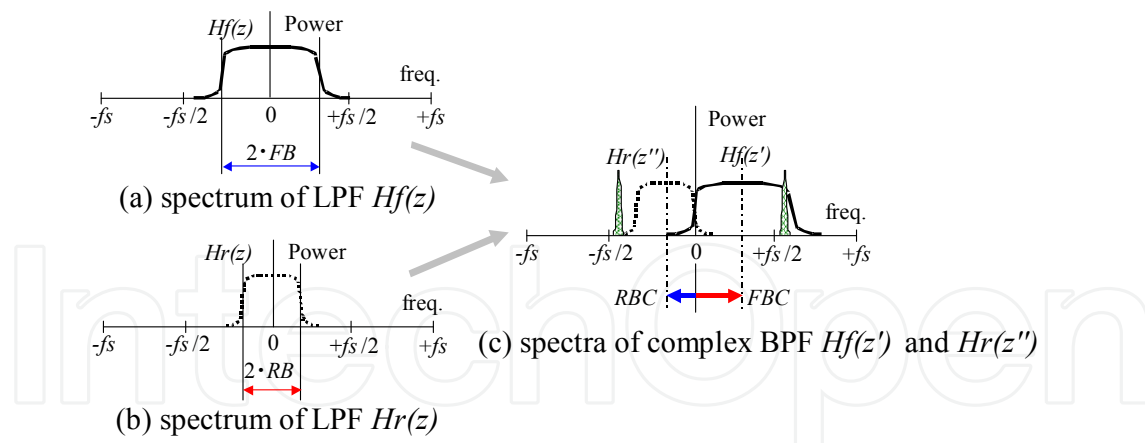


Fig. 19. Frequency design of the complex IIR filter system

4.4 Performances

To satisfy the target performances of frequency resolution and frequency characteristics shown in Table 6, we set up parameters for all the systems, such as the order of the filters and the FFT number. We use the 8th Butterworth filter with cut-off $0.495*FB*fs$ and $0.495*RB*fs$ for the LPFs of the modulation/demodulation and complex IIR filter systems. We perform 128-point FFT and 256-point inverse-FFT involved in the FFT/IFFT system, and we apply rectangular weight to $WF(\omega)$ and $WR(\omega)$.

system	estimation	delay (ms)
modulation/demodulation	$order/fs$ (*1)	2 ($order=8$)
FFT/IFFT	$0.75*N/fs$ (*2)	24 ($N=128$)
complex IIR	$order/fs$ (*1)	2 ($order=8$)

Delay is estimated at $fs=4$ kHz. (*1) not including transient response
 (*2) IFFT shift addition pitch is $N/4$.

Table 6. Time-delay of Doppler audio processing

System	calculation component	estimation equation	load (MFLOPS)
modulation/demodulation	C-add: $order*8*fs$ C-mul: $(order*8+6)*fs$ Ovh: 20%	$fs*(48*order+24)*1.2$	1.96 ($order=8$)
FFT/IFFT	C-add: $N*r1+4*N*r2$ C-mul: $N*r1/2+2*N*r2$ R-mul: $2N*6$ Ovh: 20%	$(2fs*4/N)*N*(12+6*r1+12*r2)*1.2$	5.76 ($N=128$) ($r1=7,r2=8$)
complex IIR	C-add: $order*8*fs$ C-mul: $order*8*fs$	$fs*(48*order)*1.2$	1.84 ($order=8$)

R-add: real-addition, Rmul: real-multiplication, Ovh: over head, C-add: complex-addition, C-mul: complex-multiplication, IFFT shift addition pitch is $N/4$.

Calculation volume is estimated at $fs=4$ kHz.

Table 7. Calculation load of Doppler audio processing

First, the time-delays theoretically determined from the above-mentioned parameters and calculation loads are shown in Tables 6 and 7, respectively. Since the signal processing input is sampled using f_s , delay time increases with a decrease in f_s . Table 6 shows the time-delay calculation result for a typical $f_s=4$ kHz diagnostic operation. Moreover, we simply estimate the time-delay from the calculation load itself considered to be zero by sampling, and the estimated values are not affected by the transient response. Since the operation load depends strongly on the hardware-architecture that performs signal processing, we evaluate the frequency of multiplication/addition for 1 s (single-accuracy floating point). The calculation element for every signal processing system, calculation-load estimated formula and operation load per second ($f_s=4$ kHz) are shown in Table 7. The estimated results in Tables 6 and 7 show that the complex IIR filter system and the modulation/demodulation systems are fulfilling the time-delay performance goal. Regarding the calculation load, the complex IIR filter system is the smallest, the modulation/demodulation system is slightly larger, and the FFT/IFFT system is the largest, but still small compared with previously reported values. Next, we perform a simulation to check whether we can meet the frequency feature of the performance goal in Table 4. We sweep the frequency of the input IQ-signal and measure the powers of the positive-side and negative-side outputs.

We evaluate simultaneously the frequency features and direction separation performance at this time. The frequency features of the direction separation output according to the three signal processing systems are shown in Fig. 20. A solid line denotes the positive-side component, and a dashed line, the negative-side component. The horizontal axis indicates the frequency range from $-f_s$ to $+f_s$. Moreover, the spectrum image display range corresponding to the frequency range is shown in the bottom rail. The output feature of the Doppler audio at the zero baseline-shift is shown in Figures 20(a), 20(c) and 20(e), and that of $+0.4 \cdot f_s$ baseline shift is shown in Figures 20(b), 20(d) and 20(f). From these results, we confirm that the frequency feature in each signal processing system of the Doppler audio corresponds to the baseline-shift of the spectrum image. Here, we consider that owing to the effect of the shift-addition in the Hamming window of the FFT/IFFT system, the component near DC in Figures 20(c) and 20(d) is missing. Since this missing part has a value lower than the typical setting value of cut-off frequency for the high-pass filter (equivalent to HPF in Fig. 11) of the preceding process, we do not encounter any problem. Moreover, we observe that the separation degrees of the positive-side component in Figures 20(b) and 20(f) are insufficient. We consider that the cut-off features (the 8th Butterworth filter is used in the simulation) of the modulation/demodulation and the complex IIR filter systems can be improved by making them steep. However, in the case of using an IIR filter, we should expand the internal bit length (dynamic range), because the increased load is expected to be affected by quantizing noise. For example, although Figures 20(e) and 20(f) are calculated using the single floating point (24-bit mantissa) in the simulation, by increasing cut-off frequency or filter order, mantissa bit length (accuracy) may be insufficient and the calculation load or hardware scale may increase. Although we use the Butterworth filter this time, we can choose the Chebysev filter and acquire a steep cut-off feature. On the other hand, the frequency feature and direction separation performance near cut-off frequency deteriorate with a ripple and rapid phase change.

From the above results, we observe that in choosing the response and calculation load, the complex IIR filter system is the most effective. On the other hand, the FFT/IFFT system is the most effective in choosing the frequency feature, although the response is poor. Since the

response is more important than the frequency feature clinically, and the target performance in Table 4 is fulfilled mostly, we consider the complex IIR filter system to be the best device for the direction separation of the Doppler audio system.

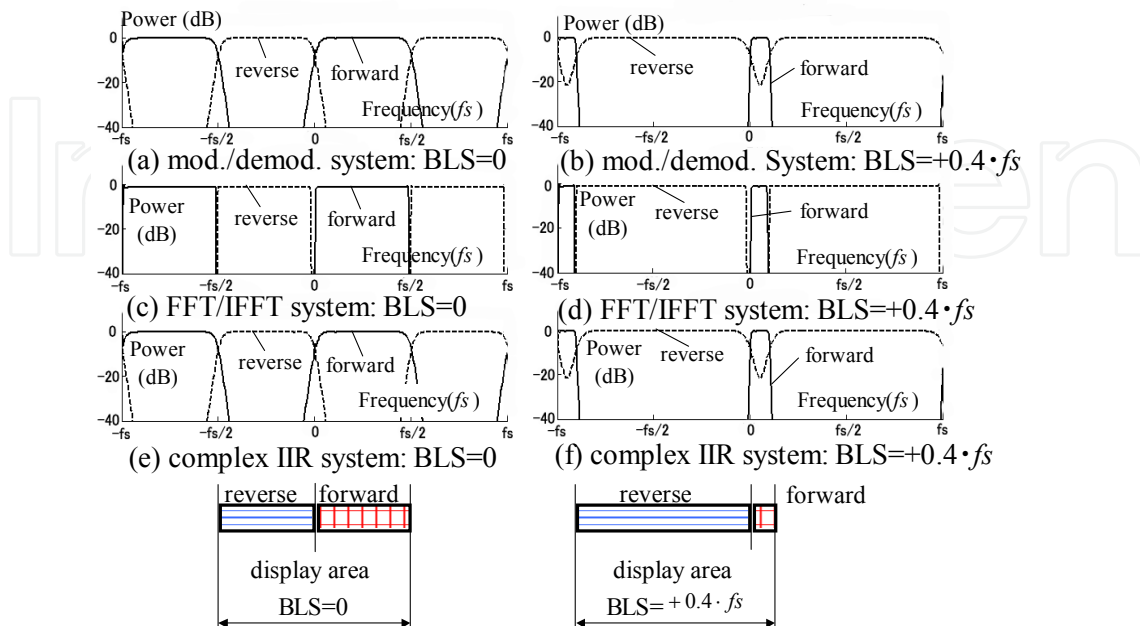


Fig. 20. Frequency characterization of Doppler audio output

4.5 Implementation of complex IIR filter system

4.5.1 Signal processing simulation

We examine the possibility of using the complex IIR filter system in signal processing simulation. The input signal is conceived to be for the actual venous blood model. The model consists of a noise component (white noise), a blood vessel wall component (clutter: low frequency high power), and a blood flow component. The powers and frequencies of these components are shown in Table 8. The input and output waveforms and power spectra of the processing blocks in the complex IIR filter system are shown in Fig. 21. The amplitude of the left-hand-side waveform is normalized by clutter amplitude to be 2. Moreover, 256-point FFT with a Hanning window is applied to the calculation of the right-hand-side power spectrum. Figures 21(a) and 21(c) show the input and output waveforms of zero insertion processing, respectively. A solid line denotes the I-component, and a dashed line, the Q-component. Figures 21(e) and 21(g) show the Doppler audio outputs of both directions at the zero baseline-shift. A solid line denotes the real component, and a dashed line, the imaginary component. Figures 21(i) and 21(k) show the Doppler audio outputs of both directions at the $+0.4 \cdot f_s$ baseline-shift. A solid line denotes the real-component, and a dashed line, the imaginary-component. Figures 21(b), 21(d), 21(f), 21(h), 21(i) and 21(l) show power spectra corresponding to the waveforms in the time domain. The aliasing spectra of blood flow and clutter are observed in Fig. 21(d) for a zero insertion processing output. Moreover, the approximately -20 dB DC component is observed at the center of the spectra. This DC component, which is not removed using the Hanning window, does not affect the latter complex band-pass filter processing. From the positive-side output waveform at the zero baseline-shift shown in Fig. 21(e), we confirm that the blood flow component of $+0.24 \cdot f_s$ frequency is separated on the positive-side. Moreover, in the power spectrum shown in Fig.

21(f) in addition to the blood flow component, we observe that the clutter component ($-0.08 \cdot f_s$) remains on the negative-side under the effect of the filter element. In the negative-side output waveform at the zero baseline-shift in Fig. 21(g), the separation of the clutter component ($-0.08 \cdot f_s$) is observed on the negative-side. Moreover, in the power spectrum in Fig. 21(h), a clutter component and a DC component are detected. When the baseline shift is $+0.4 \cdot f_s$, the spectrum image and Doppler audio must generate a negative region larger than a positive region. The positive-side output waveform after the baseline shift in Fig. 21(i) shows the disappearance of the clutter component ($+0.24 \cdot f_s$). Moreover, we confirm the absence of the blood flow component in the power spectrum shown in Fig. 21(j). We also confirm that a novel blood flow component ($-0.76 \cdot f_s$), which is an alias component ($+0.24 \cdot f_s$), is outputted into the negative-side output waveform after the baseline-shift in Fig. 21(k), except for the clutter component ($-0.08 \cdot f_s$). Moreover, in the power spectrum in Fig. 21(l), we confirm that the blood flow and clutter components are separated on the negative-side.

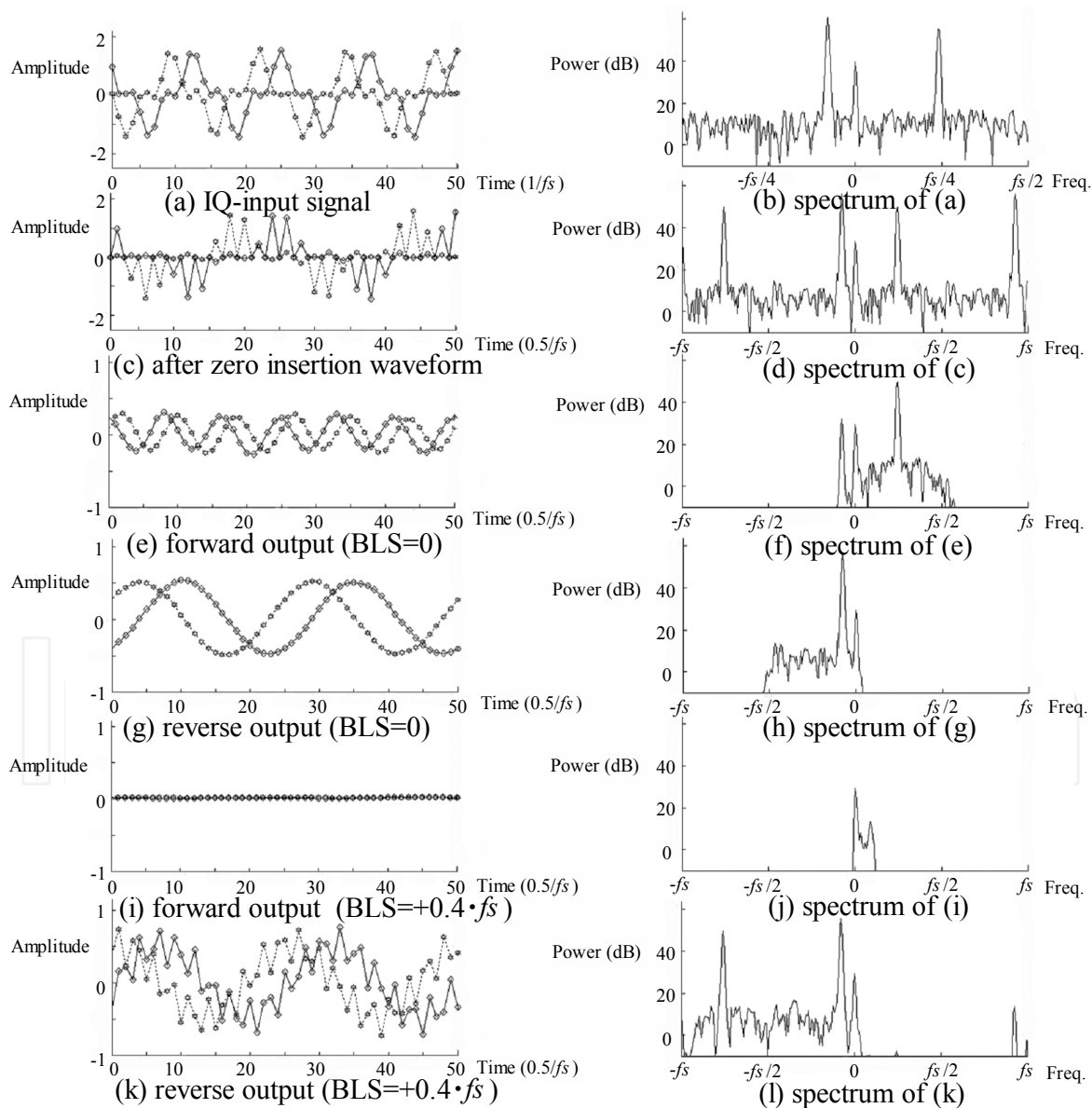


Fig. 21. Simulation waveform and spectrum of complex IIR filter system.

components	blood	noise	clutter
power	-6dB	-20dB	0dB
frequency	$0.24*fs$	(white noise)	$-0.08*fs$

Table 8. Components of simulation input model

4.5.2 Implementation

On the basis of the Doppler IQ-signal of the carotid artery collected with the actual Doppler ultrasound system, an example of anti-aliasing signal processing of the Doppler audio is shown in Fig. 22. We use a string phantom (Mark 4 Doppler Phantom: JJ&A Instrument Company) and the ultrasonic diagnosis equipment (SSA-770A: Toshiba Medical Systems Corporation) for generating and collecting the Doppler signal. We use PLT-604AT (6.0 MHz linear probe) at PRF=4 kHz equivalent to fs . We collect the IQ-data in PWD mode. Moreover, we set cut-off frequency at an HPF of 200 Hz for clutter removal. The output waveforms of both sides of the Doppler audio and spectrum image obtained from the IQ-data are shown in Fig. 22. In this figure, in the vicinity of 0.9 s, the baseline-shift is switched into $-0.4*fs$ from 0. At the zero baseline-shift, we observe aliasing in the spectrum image shown in Fig. 22(a) and a negative-side output in Fig. 22(c). However, we confirm that the positive-side display range of the spectrum image expands after a baseline-shift and is interlocked with the Doppler audio. Although it is not observed in Fig. 22, the characteristic of the band-pass filter changes immediately after a baseline-shift. We will continue to examine the transient response of the Doppler audio under this effect and to consider implementation technologies, such as muting.

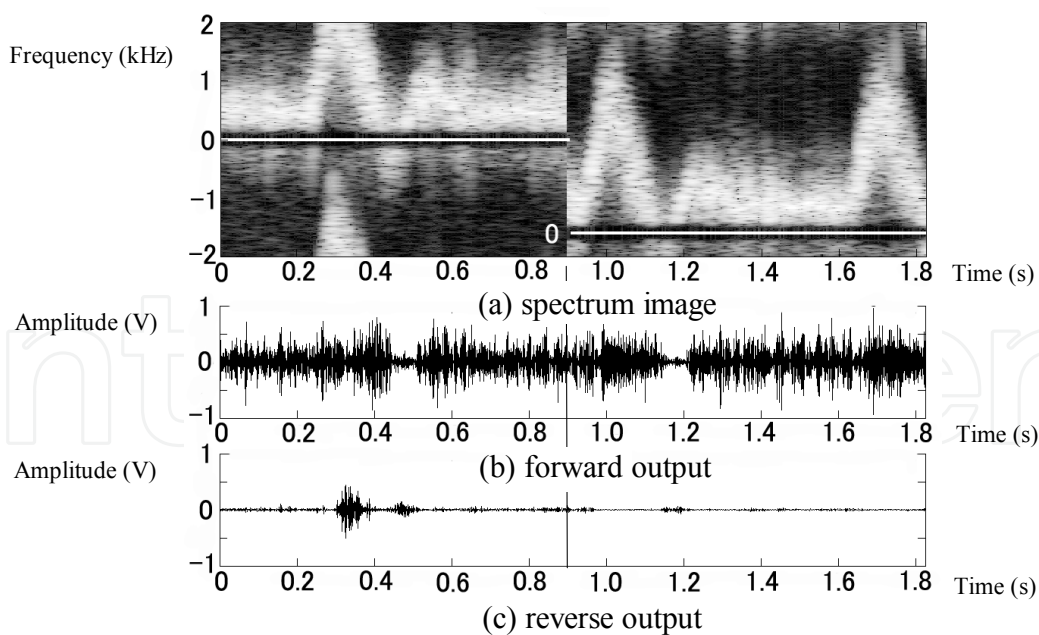


Fig. 22. Doppler spectrum display and audio output waveform

4.6 Conclusion

We developed the direction separation system of a Doppler audio interlocked with the anti-aliasing processing of a spectrum image using a complex IIR band-pass filter system.

First, we defined the target performance of Doppler audio processing and selected three signal-processing systems. We developed processing algorithms and compared their performances. Consequently, we confirmed that the complex IIR band-pass filter system has an excellent response and a low calculation load. Next, we performed functional and performance analyses by simulation with the data collected using a Doppler signal model and a phantom. Conventionally, although in the anti-aliasing process unique to a Doppler ultrasound system, the image and audio did not correspond, since it was applied only to a spectrum image, we could solve this problem by this signal processing.

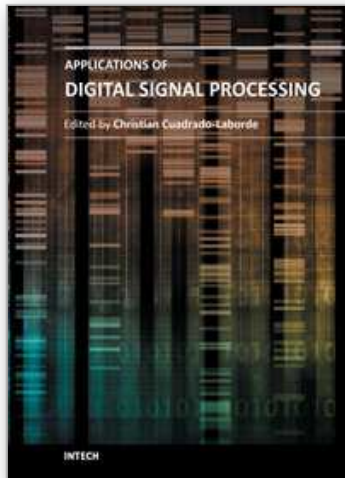
5. References

- Araki, T. (1985). *Illustration: The Communication System Theory and Reality*, Kogaku Tosho Co., Inc., Tokyo.
- Baba, T., Miyajima, Y. & Toshiba Corp. (1998). Ultrasonic diagnosis equipment, *open patent official report of Japan*, Provisional Publication No. 10-99332.
- Baba, T. & Toshiba Corp. (2002). Ultrasonic diagnostic equipment and the Doppler signal processing method, *open patent official report of Japan*, Provisional Publication of a Patent 2002-325767.
- Baba, T. (2004). The investigation of the audio direction separation in the Doppler ultrasound system Part 1: The comparison of the digital signal processing algorithm, *Proceeding of Acoust. Soc. Jpn.*, Acoustic Imaging pp.29-33.
- Baba, T. (2005). The investigation of the direction split technique of the Doppler ultrasound: Comparison of six kinds of Doppler audio processing, *J. Society of Signal Processing Applications and Technology of Japan*, Vol. 8, No. 2, pp.14-20.
- Baba, T. (2006). Investigation of the audio direction separation in Doppler ultrasound system: Signal processing of Doppler audio for aliasing, *J. Acoust. Soc. of Jpn.*, Vol. 62, No. 3, 153-160.
- Blauert, J. (1997). *Spatial hearing Revised edition*, The MIT Press, Cambridge, Massachusetts.
- Bracewell R. N. (2000). *The Fourier Transform and Its Applications*, McGraw-Hill Companies Inc., Boston.
- Cappellini, V., Constantinides, A. G. & Emiliani, P. (1983). *DIGITAL FILTERS AND THEIR APPLICATIONS (3rd edition)*, ACADEMIC PRESS INC. LTD., London
- Jensen, J. A. (1996). *Estimation of blood velocities using ultrasound: A signal processing approach*, Cambridge University Press, New York
- Jensen, J. A. (2001). A new estimator for vector velocity estimation, *IEEE transaction on UFFC*, Vol. 48, No. 4, pp.886-894.
- Koo, J., Otterson S. D. & Siemens Medical Systems Inc. (1997). Method and system for Doppler ultrasound audio dealiasing, *United States Patent US5676148*.
- Maeda, K., Sano, A., Takaie, H. & Hara, S. (2001). *Wavelet Transform and Its Application*, Asakura Publishing Co., Ltd., Tokyo.
- Mo, L. Y. L. & General Electric Company. (2001). *Method and apparatus for dynamic noise reduction for Doppler audio output*, *United States Patent US6251077*.
- Rabben, S. I. et al. (2002). Ultrasound-based vessel wall tracking: an auto-correlation technique with RF center frequency estimation, *Ultrasound in Med. & Biol.*, Vol. 28, No. 4, pp.507-517.
- Takaie H. & Tsujii S. (1995). *Multirate Signal Processing* Shokodo Co., Ltd., Tokyo.

Zhang, Y., Wang, Y. & Wang, W. (2003). Denoising quadrature Doppler signals from bi-directional flow using the Wavelet frame, *IEEE Transactions on UFFC*, Vol.50, No.5, pp561-566.

IntechOpen

IntechOpen



Applications of Digital Signal Processing

Edited by Dr. Christian Cuadrado-Laborde

ISBN 978-953-307-406-1

Hard cover, 400 pages

Publisher InTech

Published online 23, November, 2011

Published in print edition November, 2011

In this book the reader will find a collection of chapters authored/co-authored by a large number of experts around the world, covering the broad field of digital signal processing. This book intends to provide highlights of the current research in the digital signal processing area, showing the recent advances in this field. This work is mainly destined to researchers in the digital signal processing and related areas but it is also accessible to anyone with a scientific background desiring to have an up-to-date overview of this domain. Each chapter is self-contained and can be read independently of the others. These nineteenth chapters present methodological advances and recent applications of digital signal processing in various domains as communications, filtering, medicine, astronomy, and image processing.

How to reference

In order to correctly reference this scholarly work, feel free to copy and paste the following:

Baba Tatsuro (2011). Complex Digital Filter Designs for Audio Processing in Doppler Ultrasound System, Applications of Digital Signal Processing, Dr. Christian Cuadrado-Laborde (Ed.), ISBN: 978-953-307-406-1, InTech, Available from: <http://www.intechopen.com/books/applications-of-digital-signal-processing/complex-digital-filter-designs-for-audio-processing-in-doppler-ultrasound-system>

INTECH
open science | open minds

InTech Europe

University Campus STeP Ri
Slavka Krautzeka 83/A
51000 Rijeka, Croatia
Phone: +385 (51) 770 447
Fax: +385 (51) 686 166
www.intechopen.com

InTech China

Unit 405, Office Block, Hotel Equatorial Shanghai
No.65, Yan An Road (West), Shanghai, 200040, China
中国上海市延安西路65号上海国际贵都大饭店办公楼405单元
Phone: +86-21-62489820
Fax: +86-21-62489821

© 2011 The Author(s). Licensee IntechOpen. This is an open access article distributed under the terms of the [Creative Commons Attribution 3.0 License](#), which permits unrestricted use, distribution, and reproduction in any medium, provided the original work is properly cited.

IntechOpen

IntechOpen